



High-performance supercapacitors enabled by boron/nitrogen co-doped carbons through WPU/PF/GO composite

Xuxu Zhang¹ · Zitong Lin¹ · Xiaoyu Ren¹ · Chuanli Qin¹ · Qiuyu Meng¹ · Xiankai Jiang¹

Received: 14 January 2020 / Revised: 9 March 2020 / Accepted: 2 April 2020 / Published online: 27 April 2020
© Springer-Verlag GmbH Germany, part of Springer Nature 2020

Abstract

In this study, a facile one-step carbonization was developed for producing B and N co-doped carbon through waterborne polyurethane, phenolic resin, and graphene oxide composite (nWPGC) used as electrode materials in supercapacitors. Furthermore, nitrogen-enriched carbon also had repetitive urethane bond (-NHCOO) in waterborne polyurethane (nWPU). Moreover, we used the ferric chloride treatment and washing method to remove the B–N bonds. The fabricated B/N co-doped carbon had a high specific capacitance of 356.3 F g^{-1} at 0.5 A g^{-1} in 6 M KOH electrolyte, with the surface area, and pore volume ($611 \text{ m}^2 \text{ g}^{-1}$ and $0.3 \text{ cm}^3 \text{ g}^{-1}$). The assembled nWPGC-Fe-B//nWPGC-Fe-B symmetric supercapacitor exhibited an energy density of 10.35 Wh kg^{-1} was achieved at a power density of 493.2 W kg^{-1} . On top of that, the capacitor also maintained a well rate capability and brilliant cyclic stability of 89.78% capacitance retention even after 5000 cycles.

Keywords Waterborne polyurethane · Phenolic resin · Graphene oxide · Carbonization · Supercapacitor

Introduction

Supercapacitors are outstanding energy storage devices in recent years, which exhibit brilliant power density, good reversibility, and long cycle life for wide applications in high-power apparatuses [1–3]. Carbons, conductive polymers, and transition metal oxides are the major materials for supercapacitor electrode. Among them, carbons are prospective electrode due to chemical stability, which have large specific surface area, well conductivity, and abundant ion transport channels. At present, the carbon electrode materials of activated carbon, graphene, carbon nanofibers, and heteroatom doping modification carbon materials are mainly studied [4–7].

The electrochemical double-layer capacitors and pseudocapacitors are capacitive behavior of supercapacitors [8, 9]. To enhance pseudocapacitive capacitance, the method is oxidation/reduction reactions by doping heteroatoms (such

as nitrogen [10], boron [11], oxygen [12], and phosphorus [13]) in the carbon materials. Boron and nitrogen are considered the most representative elements, due to atomic radius is closest to carbon and unique electronic defects or multi-electronic properties [14–16]. B/N co-doped carbon materials can form a special electronic structure to improve the capacitor performance of supercapacitor [17–19]. Hao et al. [20] fabricated B/N co-doped carbon nanosphere frameworks as electrodes for supercapacitors (423 F g^{-1} at 0.2 A g^{-1}). Chen et al. [21] prepared B/N co-doped graphene-like carbon for capacitors (254 F g^{-1} at 0.25 A g^{-1}). Zhu et al. [22] prepared boron and nitrogen co-doped reduced graphene oxide with a high capacitance of 350 F g^{-1} at 0.5 A g^{-1} . Zhao et al. [23] prepared boron and nitrogen co-doped carbon tube bundle electrode materials exhibited excellent lithium storage performance (355 F g^{-1} at 1 A g^{-1}). Therefore, the B/N co-doped method would be a brilliant strategy to produce supercapacitor carbon materials [24–26].

Herein, we used the one-step carbonization method to produce B and N co-doped carbon from waterborne polyurethane (nWPU), phenolic resin (PF), and graphene oxide (GO). Boron and nitrogen sources came from boric acid and melamine. Furthermore, nitrogen-enriched carbon also had repetitive urethane bond (-NHCOO) in nWPU. Moreover, we used the ferric chloride treatment and washing method to remove the B–N bonds and ferric chloride results in amounts of

Electronic supplementary material The online version of this article (<https://doi.org/10.1007/s11581-020-03557-x>) contains supplementary material, which is available to authorized users.

✉ Xiankai Jiang
jiangxiankai@hlju.edu.cn

¹ School of Chemistry and Material Science, Heilongjiang University, Harbin, China

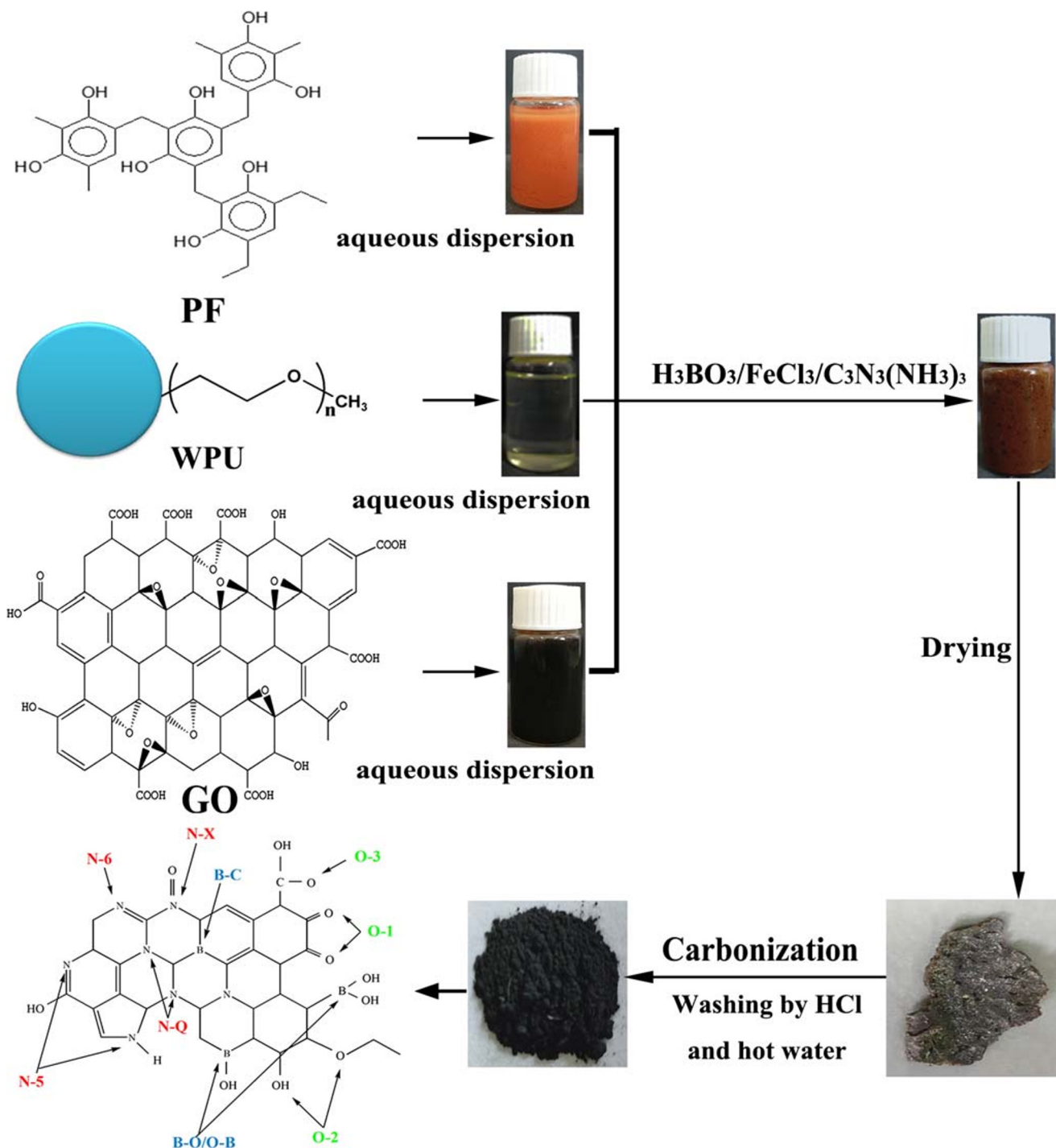


Fig. 1 Schematic illustration for synthetic procedure of nWPGC-Fe-B

micropores. The prepared B/N co-doped carbon exhibited an energy density of 10.35 Wh kg^{-1} was achieved at a power density of 493.2 W kg^{-1} . On top of that, the capacitor maintained a well rate capability and brilliant cyclic stability of 89.78% capacitance retention even after 5000 cycles. According to this, synthesis strategy will open a new way to manufacture electrode for applications in supercapacitors.

Experimental

Preparation of B/N co-doped carbon

Firstly, toluene-2,4-diisocyanate, polyethylene glycol monomethyl ether 550 (MPEG), and acetone were mixed at a stirring speed of 200 r min^{-1} in $70 \text{ }^\circ\text{C}$. They were reacted for

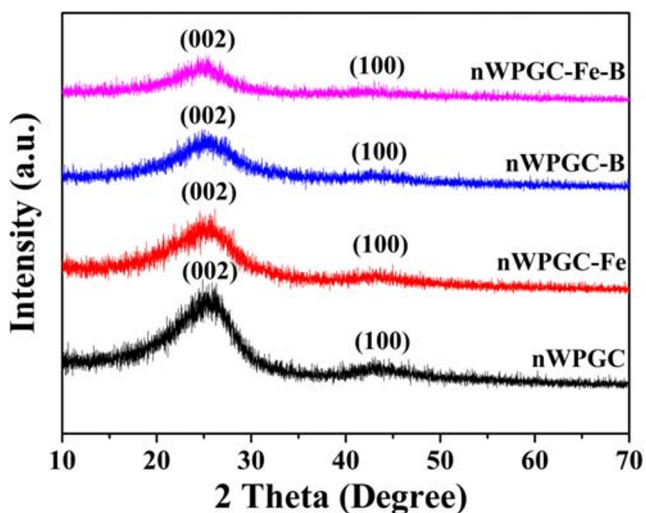


Fig. 2 XRD patterns of samples

2.5 h. Next, trimethylolpropane and melamine were putted into three-necked round-bottom. After that, we cooled down the temperature to 25 °C and emulsified with water to get nWPU. Resorcinol and formaldehyde were mixed at a stirring speed of 300 r min⁻¹ in 90 °C. Afterwards, we added solvent and catalyst into it, and reacted for 8 h to obtain PF. GO was synthesized by the modified Hummers' method [27]. In the following experiments, the phenolic resin, water polyurethane, and GO solution were mixed (in mass ratio = 5:25:1) at 25 °C to gain nWPGC. Next, ferric chloride/melamine/boric acid were added dropwise with nWPGC, respectively. The composites were ultrasonically dispersed and drying. Afterwards, the samples were heated at a rate of 5 °C min⁻¹ up to 800 °C for 2 h. In order to get rid of ferric chloride, we washed the carbon material with 6 M HCl for 3 days. It also boiled for 12 h at 80 °C to remove the boron oxide to get nWPGC-Fe-B. Use the same method to name nWPGC-B

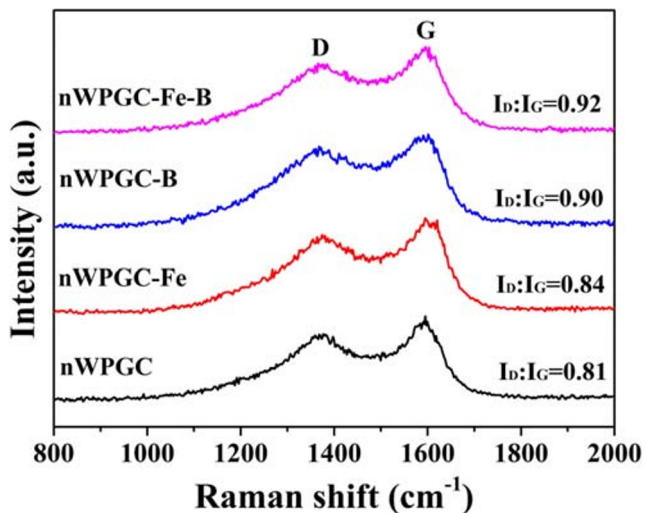


Fig. 3 Raman spectra of samples

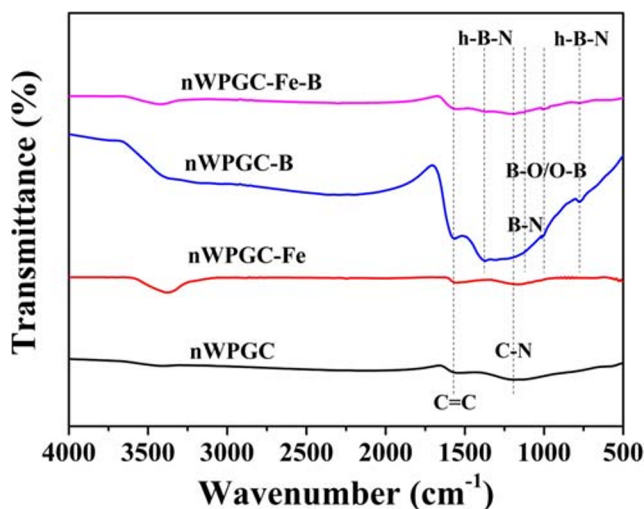


Fig. 4 FT-IR spectra of samples

and nWPGC-Fe, respectively. As shown in Fig. 1, it was the experimental procedure.

Characterization

The morphology of the samples was probed by field emission scanning electron microscope (SEM, Hitachi, S-4800, Japan) and transmission electronic microscopy (TEM, JEM-2100, JEOL Ltd., Japan). The crystal structure of samples was examined by X-ray diffraction system (XRD, Bruker, D8 Advance, Germany) equipped with Cu K α radiation. Raman spectra were determined by using a Raman spectrometer (Jobin Yvon, HR800, French). The surface element and chemical bond composition were examined by XPS and FTIR (ESCALAB 250, Thermo Fisher Scientific, UK; Bruker, Equinox 55, Germany). Porous texture parameters of samples were characterized with a physisorption analyzer (Micromeritics, ASAP 2020 HD88, USA) by N₂ adsorption/desorption measurements at 77 K. The surface area was determined by the conventional Brunauer-Emmett-Teller (BET) method and the pore size distributions were analyzed from adsorption branch isotherm by applying the density functional theory (DFT) method and assuming the slit-shaped pore model.

Electrochemical measurements

All the electrochemical performances of samples were investigated on an electrochemical workstation (CHI660D, Shanghai Chenhua, China) by a typical three-electrode system in 6 M KOH electrolyte. The negative electrode was prepared by pressing the mixture of the nWPGC-Fe-B (2 mg cm⁻²) and the polytetrafluoroethylene binder with a weight ratio of 95:5 thoroughly mixed with ethanol. The voltage window CV and GCD range from -1 to 0 V. The CV texts were investigated at scan rates ranging from 1 to 200 mV s⁻¹. The GCD test current

density ranges from 0.5 to 7 A g⁻¹. For EIS measurements, the frequency range was from 10 to 100 kHz with the amplitude of 10 mV. The specific capacitance obtained by GCD was calculated based on formula:

$$C = (I \times \Delta t) / (m \times \Delta V) \quad (1)$$

where I (A) is the current response, m (g) is the mass of the activated material, ΔV (V) is the sweep voltage, and C (F g⁻¹) is the specific capacitance.

The energy and power densities were calculated by the GCD text based on the following equations:

$$E_p = (I \times \Delta t) / (m \times \Delta V) \quad (2)$$

$$C_s \approx 4C_p \quad (3)$$

$$E_p = (C_p \times \Delta V^2) / 7.2 \quad (4)$$

$$P = (3600 \times E_p) / \Delta t \quad (5)$$

where I (A) is charge/discharge current, m (g) is the mass of the activated material, ΔV (V) is the voltage range, Δt (s) is the discharge time, C_p (F g⁻¹) is the specific capacitance, E_p (Wh kg⁻¹) is the energy density, and P (W kg⁻¹) is the power density.

Result and discussion

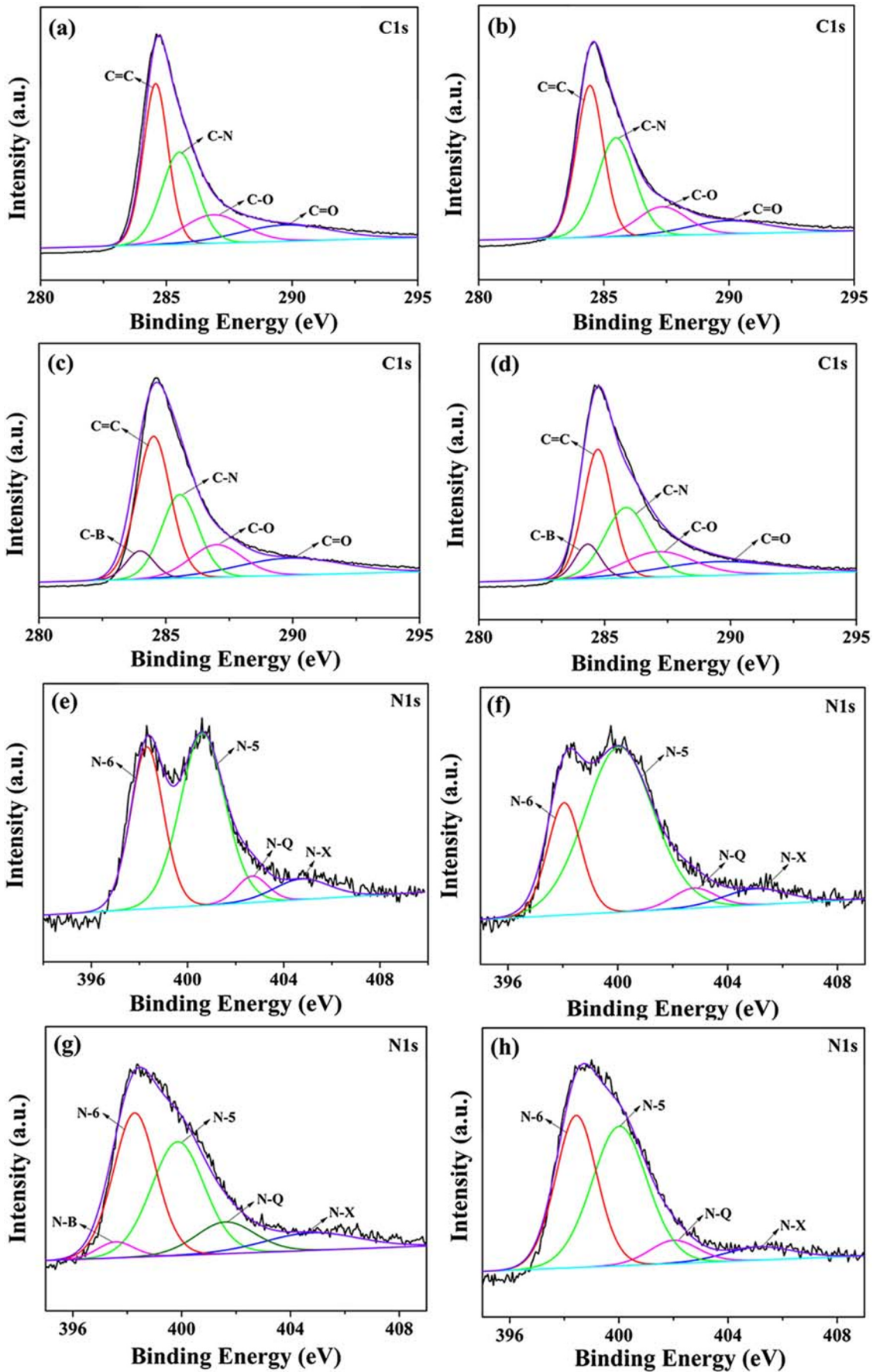
The XRD patterns of the materials are shown in Fig. 2, which exhibited two typical broad peaks at 26° (002) and 44° (100). The peak in nWPGC-B and nWPGC-Fe-B from sharp to broad indicated the decrease graphitization due to the incorporation of the heteroatoms. In comparison, nWPGC, nWPGC-Fe, nWPGC-B, and nWPGC-Fe-B had shown broader peaks at 26.10, 25.90, 25.42, and 25.16°, respectively, which also correspond to the (002) peak but shift left with larger d_{002} of 3.41, 3.44, 3.50, and 3.54 Å [28]. It could be seen from the comparison that the (002) diffraction peak shifts slightly to the left and the graphite layer spacing (d_{002}) becomes larger. It indicated that the introduction of heteroatoms including boron and nitrogen could result in change of graphite interlayer spacing [29].

The Raman spectra of samples are shown in Fig. 3. The peaks located at 1350 (G band) and 1580 cm⁻¹ (D band). They mainly represent the amorphous and the graphitized portion of carbon [22]. We compared the graphitization degree of carbon by estimating the intensity of I_D/I_G [30]. The intensity ratio of D to G band (I_D/I_G) of the nWPGC-Fe-B (0.92) and nWPGC-B (0.90) was higher than that of nWPGC-Fe (0.84) and nWPGC (0.81), suggesting the B doping would make the structural defects, which was in agreement with the XRD results.

FTIR spectra of nWPGC, nWPGC-Fe, nWPGC-B, and nWPGC-Fe-B are illustrated in Fig. 4. The nWPGC and nWPGC-Fe demonstrate functional groups at 1215 and 1558 cm⁻¹ attributed to C–N and C=C stretching vibration, respectively. The samples of nWPGC-B and nWPGC-Fe-B demonstrate the oxygen functional groups at 767/1370, 1015, 1150, 1215, and 1558 cm⁻¹ attributed to h-BN out plane bending/h-BN in-plane stretching, B–O/O–B, B–C, C–N, and C=C stretching vibrations, respectively [28, 31]. The nWPGC-Fe-B of B–N by the washing method in the characteristic signals of 767 cm⁻¹ became weak. We could reduce the B–N bonds to improve electrochemical performance, which confirm by the following electrochemical tests.

The XPS spectra of nWPGC, nWPGC-Fe, nWPGC-B, and nWPGC-Fe-B are shown in Fig. 5. The content in carbon network surface elemental content is shown in Table 1, which shows the B and N atom was successfully doped into the carbon structure. As shown in Fig. 5o, the XPS spectra of nWPGC, nWPGC-Fe, nWPGC-B, and nWPGC-Fe-B have four main peaks at 190.2 eV, 284.3 eV, 398.2 eV, and 532.4 eV that belong to B1s, C1s, N1s, and O1s, respectively. The C1s peak (Fig. 5a–d) was fitted by five component peaks, namely, C–C (284.6 eV), C–N (286.5 eV), C–O (287.1 eV), C=O (287.9 eV), and C–B (283.9 eV) [19]. The N1s peak (Fig. 5e–h) revealed that the doped N atoms existed in the form of pyridinic N (N-6, 398.7 eV), pyrrolic N (N-5, 399.8 eV), graphitic N (N-Q, 400.9 eV), and N-oxide (N-X, 402.8 eV) [24]. These nitrogen-based groups could help produce pseudocapacitance, which enhance the conductivity and wettability of this kind of electrode materials [32, 33]. The O1s spectrum (Fig. 5i–l) could be deconvoluted into four peaks which were from carbonyl functional groups (O-1, 531.5 eV), phenol groups, and/or C–O–C ether groups (O-2, 532.4 eV), O–B, (533.2 eV), and O=C–OH carboxylic groups (O-3/534.3 eV) [19]. The B1s spectrum (Fig. 5m, n) could be ascribed to three components, including B–C (190.5 eV), B–N (191.7 eV), and B–O (192.8 eV) [34]. The most important species affecting energy storage performance may be negatively charged N-6, N-5, B-C, and O-2. Relative surface concentrations of N, B, and O species obtained from the N1s, O1s, and B1s core-level peak analyses are summarized in Table 2. Furthermore, nWPGC-Fe-B presents much active N-5 (48.22 at%), N-6 (39.07 at%), B-C (69.54 at%), and O-2 (54.08 at%), contributing to increase of pseudocapacitance. Obviously, the percentage of nWPGC-B and nWPGC-Fe-B

Fig. 5 High resolution XPS spectra of: N1s in **a** nWPGC, **b** nWPGC-Fe, **c** nWPGC-B, **d** nWPGC-Fe-B; N1s in **e** nWPGC, **f** nWPGC-Fe, **g** nWPGC-B, **h** nWPGC-Fe-B; O1s in **i** nWPGC, **j** nWPGC-Fe, **k** nWPGC-B, **l** nWPGC-Fe-B; B1s in **m** nWPGC-B, **n** nWPGC-Fe-B. **o** XPS survey spectra



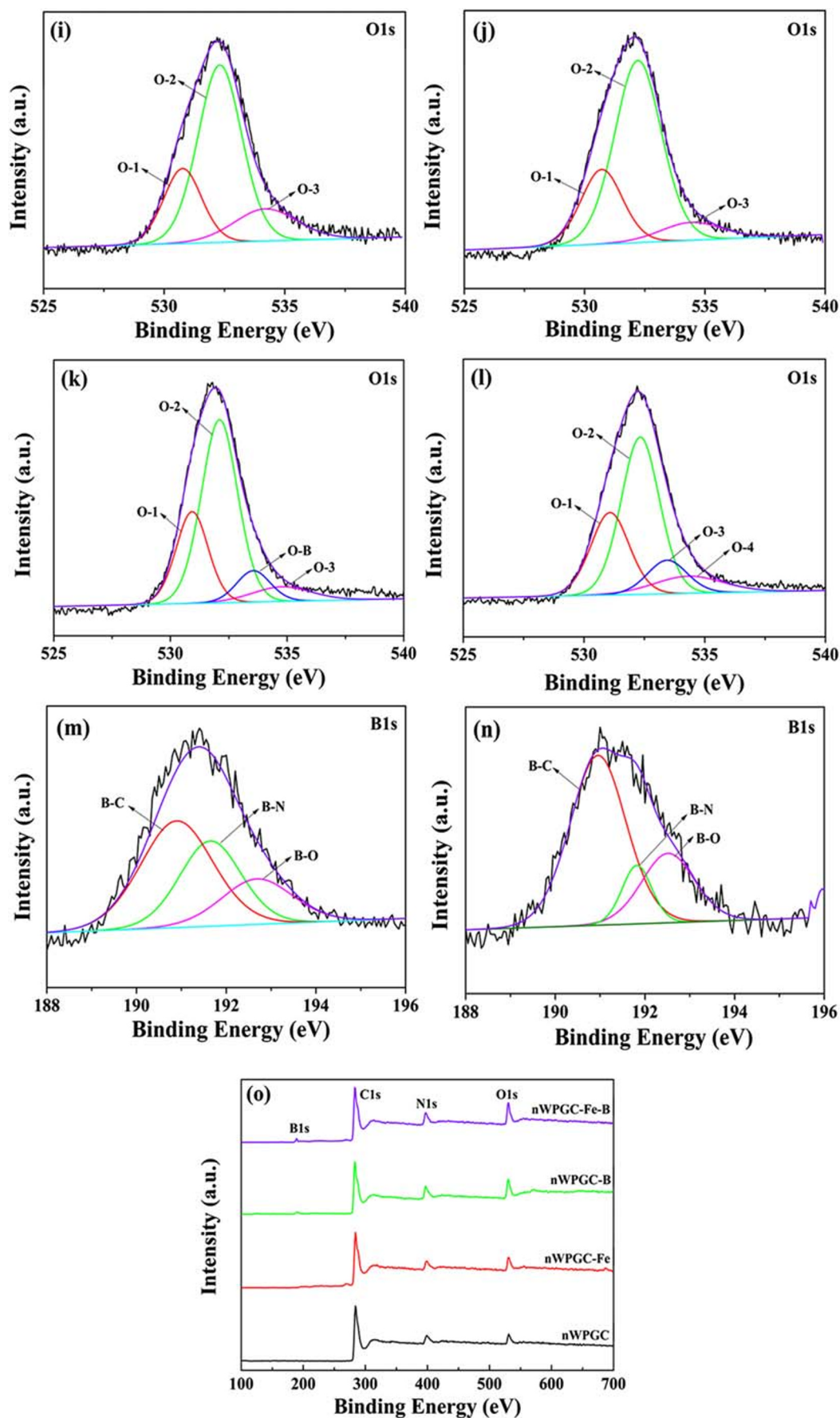


Fig. 5 continued.

Table 1 Physical and electrochemical properties of samples

| | | Samples | | | |
|--|---|---------|----------|---------|------------|
| | | nWPGC | nWPGC-Fe | nWPGC-B | nWPGC-Fe-B |
| SBET ^[a] (m ² g ⁻¹) | | 7 | 236 | 289 | 611 |
| V _{total} ^[b] (cm ³ g ⁻¹) | | 0.0 | 0.1 | 0.2 | 0.3 |
| D _{avg} ^[c] (nm) | | 12.7 | 1.7 | 3.5 | 2.0 |
| V _{mic} ^[d] (cm ³ g ⁻¹) | | 0.0 | 0.1 | 0.0 | 0.1 |
| V _{mec+mac} ^[e] (cm ³ g ⁻¹) | | 0.05 | 0.02 | 0.2 | 0.2 |
| Concent ^[f] (at%) | C | 85.5 | 84.5 | 75.7 | 75.9 |
| | N | 9.0 | 8.3 | 12.6 | 12.1 |
| | O | 7.2 | 7.6 | 8.2 | 8.0 |
| | B | 0.0 | 0.0 | 4.1 | 4.1 |

^[a]The specific surface areas were calculated using the BET method

^[b]Total pore volume at P/P₀ = 0.99

^[c]Average pore diameter

^[d]Micropore volume

^[e]Mesopore volume and macropore volume

^[f]Elemental contents of samples

compared with the B–N bond decreased from 32.38 at% to 13.60 at%. This fully illustrated that after the boric acid treatment, B atoms were more likely to bind with N atoms and formed B–N bond. Treatment with ferric chloride could effectively suppress the formation of B–N bonds, and it is more

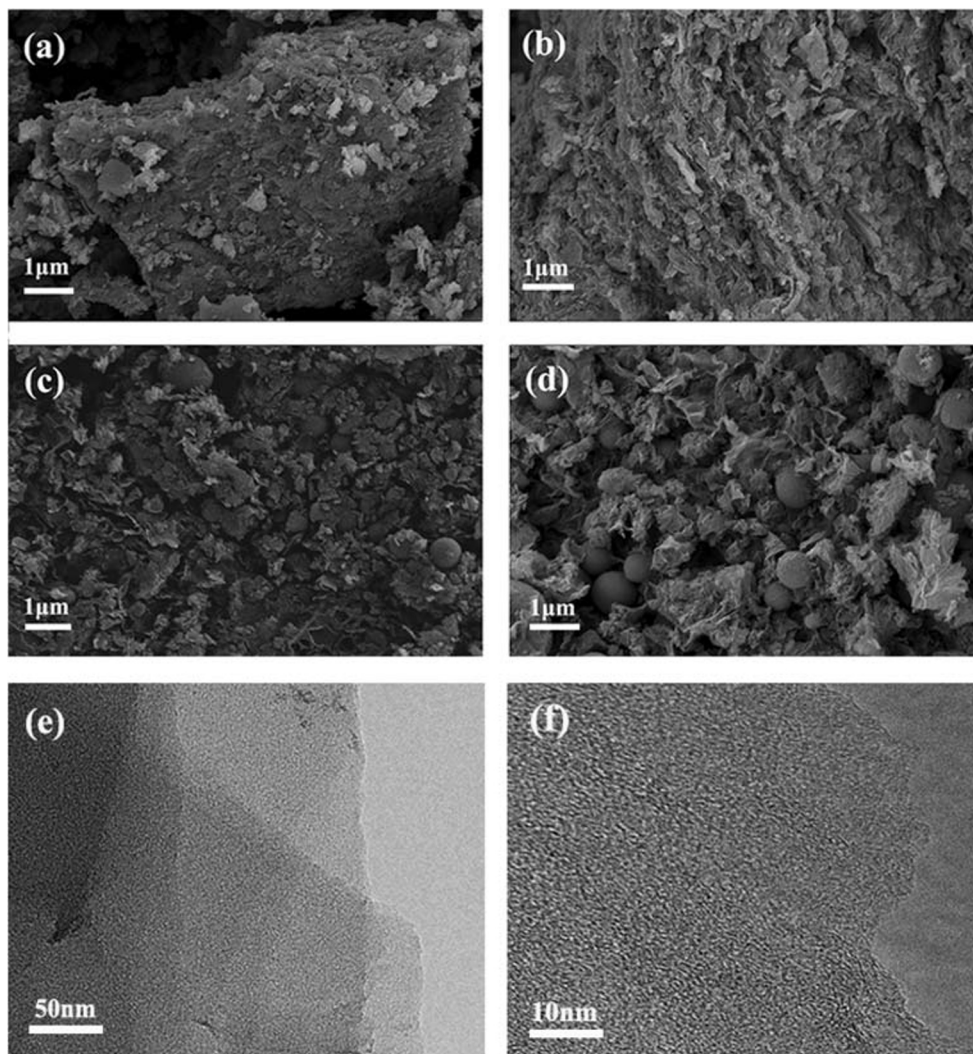
favorable to bind with carbon atoms. So, nWPGC-Fe-B has higher pseudocapacitive performance due to effective B–C bond was formed.

The SEM images of nWPGC, nWPGC-Fe, nWPGC-B, and nWPGC-Fe-B are shown in Fig. 6. Figure 6a had shown

Table 2 Relative concentrations of C, N, O, and B

| | | Samples | | | |
|-----------------------|------|---------|----------|---------|------------|
| | | nWPGC | nWPGC-Fe | nWPGC-B | nWPGC-Fe-B |
| C configuration (at%) | C=C | 38.17 | 40.02 | 39.49 | 33.98 |
| | C-N | 31.17 | 35.86 | 13.91 | 27.22 |
| | C-O | 16.19 | 13.75 | 14.76 | 15.96 |
| | C=O | 14.47 | 10.38 | 25.29 | 14.96 |
| | C-B | 0 | 0 | 6.55 | 7.89 |
| N configuration (at%) | N-6 | 35.35 | 22.16 | 39.54 | 39.07 |
| | N-5 | 51.56 | 66.73 | 37.65 | 48.22 |
| | N-Q | 5.46 | 5.04 | 11.44 | 7.06 |
| | N-X | 7.36 | 6.08 | 10.16 | 5.65 |
| | N-B | 0 | 0 | 3.56 | 0 |
| O configuration (at%) | O-1 | 22.57 | 24.29 | 25.54 | 27.07 |
| | O-2 | 61.38 | 67.02 | 57.74 | 54.08 |
| | O-3 | 16.05 | 8.69 | 7.54 | 10.12 |
| | O-B | 0 | 0 | 9.19 | 11.41 |
| B configuration (at%) | BC3 | 0 | 0 | 47.66 | 69.54 |
| | BC2O | 0 | 0 | 19.96 | 18.64 |
| | B-N | 0 | 0 | 32.38 | 11.82 |

Fig. 6 SEM images of **a** nWPGC, **b** nWPGC-Fe, **c** nWPGC-B, and **d** nWPGC-Fe-BN. TEM images of nWPGC-Fe-B (**e**, **f**)



a massive carbon structure and some small carbon particles. We used the acid and water washing method to remove the ferric chloride catalyst, and the nWPGC-Fe (Fig. 6b) could see the laminar structure appearing on the block. The nWPGC-B

(Fig. 6c) had a clear pore structure, and the massive structure reveals the spherical morphology of phenolic. It became rough on the surface, which with irregular carbon particle. The phenolic spheres and some pore structures had been clearly

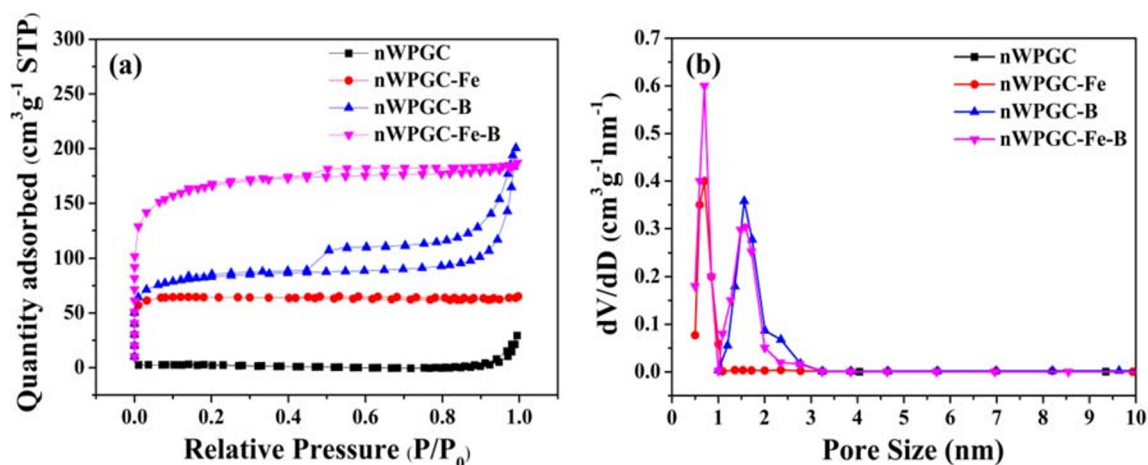


Fig. 7 **a** N₂ absorption/desorption isotherms and **b** pore size distributions of the samples

displayed from WPGC-Fe-B (Fig. 6d). It could also be proven from the BET test. This phenomenon means that this disordered pore structure could provide myriads of interconnected channels to decrease the electrolyte ion diffusion distance during the charge-discharge process, which is good for electrode material to enhance the EDLC [34, 35]. Figures 6e and f show the TEM images of nWPGC-Fe-B at different magnification. From the TEM images, there were abundant worm-like micropores on the surface of WPGC-Fe-B [36–38]. It was in consistent with the results of N_2 adsorption-desorption shown in Fig. 7. The porous structure provides a large number for storage to electrolyte ion, which could improve the capacitive performance.

Figure 7a shows the N_2 adsorption/desorption isotherm of the nWPGC, nWPGC-Fe, nWPGC-B, and nWPGC-Fe-B particles. In Fig. 7a, nWPGC-Fe-B exhibited a combined IV curve, which indicated the coexistence of micropores and mesopores [39, 40]. The pore size distribution (Fig. 7b) of nWPGC-Fe-B revealed abundant micropores and mesopores focused on 0.5–3.5 nm, which contribute to the ion transport and achieving high electric double-layer capacitance [41, 42]. Such structure of nWPGC-Fe-B has high BET surface area and pore volume up to $611 \text{ m}^2 \text{ g}^{-1}$ and $0.3 \text{ cm}^3 \text{ g}^{-1}$ (Table 1) [43]. Evidently, ferric chloride washing treatment results in large amounts of micropores. In addition, adding boric acid could also increase the content of micropores and mesopores suggesting that the water-soluble boron oxides eliminated by washing process. Such porous structures were expected to be perfect electrode materials used in supercapacitors [28].

We investigated the electrochemical behavior of samples in 6 M KOH electrolyte by three-electrode system shown in Fig. 8. Figure 8a shows the CV text of samples at a scan rate of 1 mV s^{-1} , which all reveal as rectangular-like characteristic curve. However, nWPGC-B and nWPGC-Fe-B showed obvious broad redox peak, indicating that heteroatom B contributed an indispensable pseudocapacitance. The cyclic CV text of nWPGC-Fe-B (Fig. 8b) was exhibited at $1\text{--}200 \text{ mV s}^{-1}$ scan rates. It was shown that the material has excellent rate performance and good reversibility. The nWPGC-Fe-B-900 of CV

text (Fig. 8c) was prepared by heat-treating nWPGC-Fe-B at $900 \text{ }^\circ\text{C}$ for 2 h in a nitrogen atmosphere to reduce heteroatoms. Due to high heat treatment of the material, it could be clearly noticed that reduced the specific capacitance and the CV curve was transformed into a narrower rectangular shape.

All the GCD texts (Fig. 8d) were symmetric, showing regularly shapes, implying well reversibility and excellent Coulombic efficiency. Specific charge and discharge branches could be seen in Fig. S1a and b. It was shown that the discharge time of nWPGC-B and nWPGC-Fe-B was longer, which proved that the contribution of element B to the capacitor was indispensable. It was consistent with the result in Fig. 8a. The constant current charge-discharge test of nWPGC-Fe-B at different current densities is shown in Fig. 8e. The material has a lower internal resistance, which corresponds to the result of AC impedance. The relationship curve between specific capacitance and current density is shown in Fig. 8f and Table 3. The nWPGC-Fe-B has a large current density even in 7 A g^{-1} ; its specific capacitance value could still be maintained at 244.5 F g^{-1} , which had good charge and discharge performance and capacitance behavior.

The EIS measurement (Fig. 8g) investigated the impedance of materials. The corresponding equivalent circuit was displayed in Fig. 8h. Table 4 shows the fitting results for all samples. The solution resistance of all samples was less than $1.0 \text{ } \Omega$, which indicated low solution resistance. The charge transfer resistances R_{ct} of nWPGC, nWPGC-Fe, nWPGC-B, and nWPGC-Fe-B were 3.054, 1.782, 1.349, and 0.777, respectively. The nWPGC-Fe-B has lowest charge transfer resistance R_{ct} , indicated that it had faster charge transfer characteristics [44, 45]. Therefore, we knew that nWPGC-Fe-B had better conductivity, fast charge transfer, and electrolyte ion diffusion characteristics, which lead to better electrochemical performance. In Fig. 8i, j, it is suggested that nWPGC-Fe-B could remain 94.8% initial capacitance after 3000 cycles, and the CV text of nWPGC-Fe-B did not present evident distortion. Table 3 compares the performance of the nWPGC-Fe-B composite with the previously reported carbon electrode materials [10, 28, 29, 34, 46–49].

Table 3 Specific capacitance of the carbon electrode materials of supercapacitors for the comparison with nWPGC-Fe-B in this study

| Sample | Electrolyte | Current density (A g^{-1}) | Capacitance (F g^{-1}) | Ref. |
|------------------------|-----------------------------|---------------------------------------|-----------------------------------|----------|
| nWPGC-Fe-B | 6 M KOH | 0.5 | 356.3 | In work |
| RGO-AgNP/N-CNF | 6 M KOH | 0.5 | 188 | [10] |
| BNOC-BU-W | 6 M KOH | 0.5 | 238 | [28] |
| WPU-GO-Fe-B | 6 M KOH | 0.5 | 330 | [29] |
| NCF (Fe) | 6 M KOH | 0.5 | 273.7 | [34] |
| EDTANa ₂ Zn | 6 M KOH | 0.1 | 229 | [40, 46] |
| CNBs | 1 M H_2SO_4 | 0.2 | 299.4 | [41, 47] |
| 3D-BN-CNF-ZF900 | 2 M KOH | 0.5 | 295 | [42, 48] |
| Graphene/PU | 1 M H_2SO_4 | 0.5 | 218 | [43, 49] |

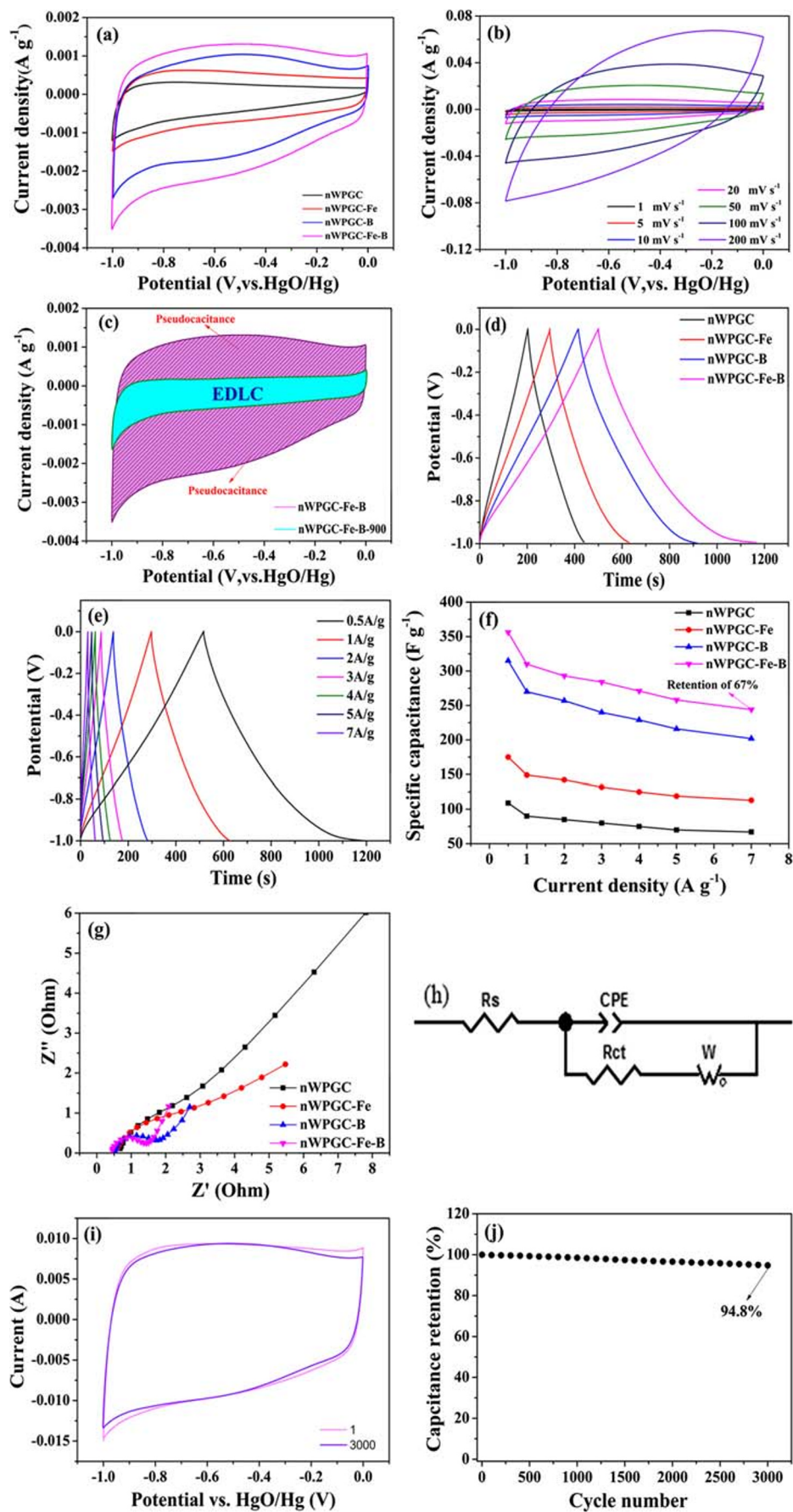


Fig. 8 Electrochemical evaluations of samples in three-electrode configuration: **a** CV text at 1 mV s⁻¹, **b** CV text of nWPGC-Fe-B at 1–200 mV s⁻¹, **c** CV text of nWPGC-Fe-B and nWPGC-Fe-B-900 at 1 mV s⁻¹. **d** GCD text at 0.5 A g⁻¹, **e** GCD text of nWPGC-Fe-B at 0.5–7 A g⁻¹. **f** Comparative capacitance retentions at the corresponding current density. **g** Nyquist plots. **h** Equivalent circuit. **i** CV text of nWPGC-Fe-B at 1–3000 th cycles at 20 mV s⁻¹. **j** The capacitance retention of nWPGC-Fe-B

Based on the outstanding electrochemical performance of nWPGC-Fe-B, we have prepared a symmetrical supercapacitor to evaluate its practical application value. The specific capacitance was revealed from the GCD text (Fig. 9a). The resultant specific capacitances were approximately 76.5 F g⁻¹ at 1 A g⁻¹. In Fig. 9b, we could clearly saw the excellent electron migration efficiency of the device, which could still remain at 79.7% even

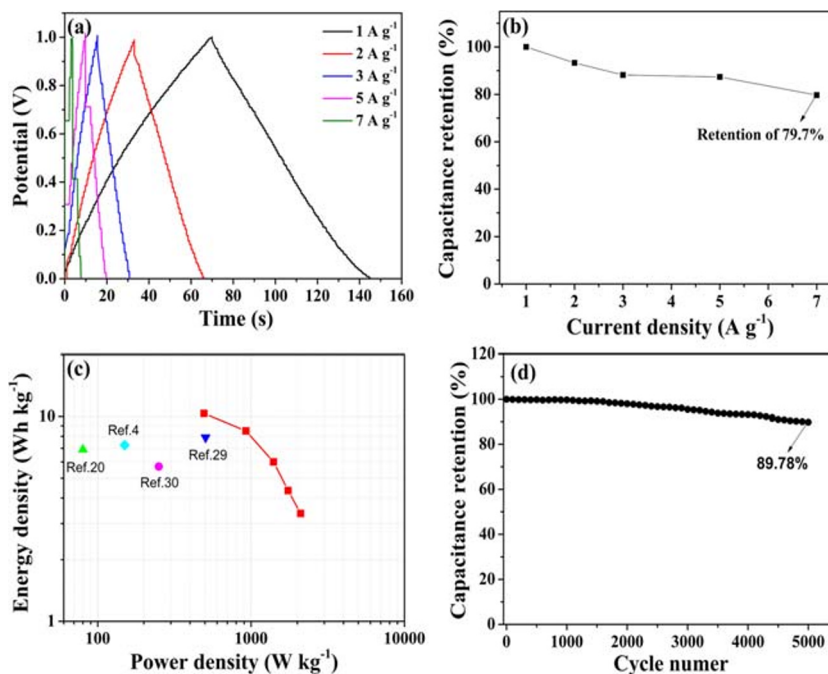
at a current density of 7 A g⁻¹. According to Fig. 9c, it was exhibited a maximum energy density of 10.35 Wh kg⁻¹ at a power density of 493.2 W kg⁻¹, and at a power density of 2101 W kg⁻¹, the energy density was maintained at 3.36 W h kg⁻¹. Our result was better than that reported for several heteroatom-doped carbon materials such as nitrogen-doped hierarchical porous carbon, B/N co-doped carbon nanosphere, boron/nitrogen co-doped carbon, and N and S dual-doped porous carbon [4, 20, 29, 30]. Another key factor in evaluating supercapacitors is the cycle stability test. Figure 9d shows the long-term cycling performance test of the device at a current density of 5 A g⁻¹. Even after 5000 cycles, the initial capacity of 89.78% could be retained. As a result, this material has excellent electrochemical performance as a new generation of supercapacitors.

Table 4 Selected EIS fitting results for the nWPGC, nWPGC-Fe, nWPGC-B, and nWPGC-Fe-B samples

| Equivalent circuit elements | Samples | | | |
|-----------------------------|-----------|-----------|-----------|------------|
| | nWPGC | nWPGC-Fe | nWPGC-B | nWPGC-Fe-B |
| R_s (Ω) | 0.72823 | 0.60802 | 0.52897 | 0.44734 |
| CPE_T | 0.0052823 | 0.0017769 | 0.0028268 | 0.0010271 |
| CPE_P | 0.80926 | 0.78722 | 0.77192 | 0.75863 |
| R_{ct} (Ω) | 3.054 | 1.782 | 1.349 | 0.777 |
| W_R | 9.614 | 4.782 | 2.411 | 1.219 |
| W_T | 0.65963 | 0.46156 | 0.34408 | 0.21613 |
| W_P | 0.34981 | 0.28129 | 0.28057 | 0.16521 |

CPE_T is the capacitance when $CPE_P = 1$; CPE_P is the constant phase element exponent; W_R is the diffusion resistance (Warburg diffusion resistance); W_T is the diffusion time constant; W_P is a fractional exponent between 0 and 1

Fig. 9 In a two-electrode system: **a** GCD text at 1–7 A g⁻¹, **b** rate capability at different current densities, **c** Ragone plot of nWPGC-Fe-B symmetrical supercapacitor, and **d** cycling stability at the current density of 5 A g⁻¹



Conclusions

In a word, the boron and nitrogen co-doping carbon materials have been synthesized by one-step carbonization from nWPGC as electrode materials for supercapacitors. Boron and nitrogen sources come from boric acid and melamine, respectively. Furthermore, nitrogen-enriched carbon also had repeating urethane bond (-NHCOO) in waterborne polyurethane (nWPU). Moreover, we used the ferric chloride treatment and washing method to remove the B–N bonds and ferric chloride results in amounts of micropores. The fabricated B/N co-doped carbon had a high specific capacitance of 356.3 F g^{-1} at 0.5 A g^{-1} in 6 M KOH electrolyte, with the surface area, and pore volume ($611 \text{ m}^2 \text{ g}^{-1}$ and $0.3 \text{ cm}^3 \text{ g}^{-1}$). In a two-electrode system, it exhibited an energy density of 10.35 Wh kg^{-1} and was achieved at a power density of 493.2 W kg^{-1} . More importantly, the capacitor also maintained a well rate capability and notable cyclic stability of 89.78% capacitance retention even after 5000 charge-discharge cycles. According to this, the synthesis strategy will open a new way to manufacture electrode for applications in supercapacitors.

Acknowledgments The authors are grateful to the support of the National Natural Science Foundation of China (grant no. 21372067) and Innovation Research Project of Postgraduate of Heilongjiang University (YJSCX2019-186HLJU).

References

- Huang CH, Zhang Q, Chou TC, Chen CM, Su DS, Doong RA (2012) Three-dimensional hierarchically ordered porous carbons with partially graphitic nanostructures for electrochemical capacitive energy storage. *ChemSusChem* 5:563–571. <https://doi.org/10.1002/cssc.201100618>
- Wang G, Zhang J, Kuang S, Zhou J, Xing W, Zhuo S (2015) Nitrogen-doped hierarchical porous carbon as an efficient electrode material for supercapacitors. *Electrochim Acta* 153:273–279. <https://doi.org/10.1016/j.electacta.2014.12.006>
- Zhao Z, Xie Y (2018) Electrochemical supercapacitor performance of boron and nitrogen co-doped porous carbon nanowires. *J Power Sources* 400:264–276. <https://doi.org/10.1016/j.jpowsour.2018.08.032>
- Geng Q, Huang G, Liu Y, Li Y, Liu L, Yang X, Wang Q, Zhang C (2019) Facile synthesis of B/N co-doped 2D porous carbon nanosheets derived from ammonium humate for supercapacitor electrodes. *Electrochim Acta* 298:1–13. <https://doi.org/10.1016/j.electacta.2018.12.038>
- Yun YS, Park MH, Hong SJ, Lee ME, Park YW, Jin HJ (2015) Hierarchically porous carbon nanosheets from waste coffee grounds for supercapacitors. *ACS Appl Mater Interfaces* 7:3684–3690. <https://doi.org/10.1021/am5081919>
- Hao Q, Xia X, Lei W, Wang W, Qiu J (2015) Facile synthesis of sandwich-like polyaniline/boron-doped graphene nano hybrid for supercapacitors. *Carbon* 81:552–563. <https://doi.org/10.1016/j.carbon.2014.09.090>
- Zhang Q, Wang Y, Zhang B, Zhao K, He P, Huang B (2018) 3D superelastic graphene aerogel-nanosheet hybrid hierarchical nanostructures as high-performance supercapacitor electrodes. *Carbon* 127:449–458. <https://doi.org/10.1016/j.carbon.2017.11.037>
- Cheng C, He S, Zhang C, Du C, Chen W (2018) High-performance supercapacitor fabricated from 3D free-standing hierarchical carbon foam-supported two dimensional porous thin carbon nanosheets. *Electrochim Acta* 290:98–108. <https://doi.org/10.1016/j.electacta.2018.08.081>
- Hu Y, Shen L, Wei X, Long Z, Guo X, Qiu X (2019) One-pot synthesis of novel B, N co-doped carbon materials for high-performance sodium-ion batteries. *ChemistrySelect* 4:6445–6450. <https://doi.org/10.1002/slct.201900950>
- Cai N, Fu J, Zeng H, Luo X, Han C, Yu F (2018) Reduced graphene oxide-silver nanoparticles/nitrogen-doped carbon nanofiber composites with meso-microporous structure for high-performance symmetric supercapacitor application. *J Alloys Compd* 742:769–779. <https://doi.org/10.1016/j.jallcom.2018.01.011>
- Lu Y, Li Z, Bai Z, Mi H, Ji C, Pang H, Yu C, Qiu J (2019) High energy-power Zn-ion hybrid supercapacitors enabled by layered B/N co-doped carbon cathode. *Nano Energy*:66. <https://doi.org/10.1016/j.nanoen.2019.104132>
- He D, Niu J, Dou M, Ji J, Huang Y, Wang F (2017) Nitrogen and oxygen co-doped carbon networks with a mesopore-dominant hierarchical porosity for high energy and power density supercapacitors. *Electrochim Acta* 238:310–318. <https://doi.org/10.1016/j.electacta.2017.03.218>
- Wang T, Zhang J, Hou Q, Wang S (2019) Utilization of nutrient rich duckweed to create N, P Co-doped porous carbons for high performance supercapacitors. *J Alloys Compd* 771:1009–1017. <https://doi.org/10.1016/j.jallcom.2018.08.295>
- Zhang D, Wang J, Wang Q, Huang S, Feng H, Luo H (2019) Nitrogen self-doped porous carbon material derived from metal-organic framework for high-performance super-capacitors. *J Energy Storage* 25. <https://doi.org/10.1016/j.est.2019.100904>
- Sun F, Wu HB, Liu X, Liu F, Han R, Qu Z, Pi X, Wang L, Gao J, Lu Y (2018) A high-rate and ultrastable anode enabled by boron-doped nanoporous carbon spheres for high-power and long life lithium ion capacitors. *Mater Today Energy* 9:428–439. <https://doi.org/10.1016/j.mtener.2018.07.009>
- Qiu S, Chen Z, Zhuo H, Hu Y, Liu Q, Peng X, Zhong L (2019) Using FeCl₃ as a solvent, template, and activator to prepare B, N co-doping porous carbon with excellent supercapacitance. *ACS Sustain Chem Eng* 7:15983–15994. <https://doi.org/10.1021/acssuschemeng.9b02431>
- Mazanek V, Matejkova S, Sedmidubsky D, Pumera M, Sofer Z (2018) One-step synthesis of B/N co-doped graphene as highly efficient electrocatalyst for the oxygen reduction reaction: synergistic effect of impurities. *Chemistry* 24:928–936. <https://doi.org/10.1002/chem.201704515>
- Thakur AK, Majumder M, Choudhary RB, Singh SB (2018) MoS₂ flakes integrated with boron and nitrogen-doped carbon: striking gravimetric and volumetric capacitive performance for supercapacitor applications. *J Power Sources* 402:163–173. <https://doi.org/10.1016/j.jpowsour.2018.09.029>
- Zhang X, Lin Z, Qin C, Guo X, Ma Y, Jiang X (2019) One-step carbonization production of B/N co-doped carbon from polyurethane/phenolic/GO composite for supercapacitors. *J Mater Sci Mater Electron*. <https://doi.org/10.1007/s10854-019-02579-0>
- Hao J, Wang J, Qin S, Liu D, Li Y, Lei W (2018) B/N co-doped carbon nanosphere frameworks as high-performance electrodes for supercapacitors. *J Mater Chem A* 6:8053–8058. <https://doi.org/10.1039/c8ta00683k>

21. Chen Z, Hou L, Cao Y, Tang Y, Li Y (2018) Gram-scale production of B, N co-doped graphene-like carbon for high performance supercapacitor electrodes. *Appl Surf Sci* 435:937–944. <https://doi.org/10.1016/j.apsusc.2017.11.159>
22. Zhu T, Li S, Ren B, Zhang L, Dong L, Tan L (2019) Plasma-induced synthesis of boron and nitrogen co-doped reduced graphene oxide for super-capacitors. *J Mater S* 54:9632–9642. <https://doi.org/10.1007/s10853-019-03552-2>
23. Zhao J, Li Y, Wang G, Wei T, Liu Z, Cheng K, Ye K, Zhu K, Cao D, Fan Z (2017) Enabling high-volumetric-energy-density supercapacitors: designing open, low-tortuosity heteroatom-doped porous carbon-tube bundle electrodes. *J Mater Chem A* 5:23085–23093. <https://doi.org/10.1039/c7ta07010a>
24. Liu K, Xu J, Wang Y, Qian M, Zhao W, Zeng Y, Huang F (2019) Boron and nitrogen co-doped trimodal-porous wood-derived carbon for boosting capacitive performance. *Energy Technol-Ger* 8. <https://doi.org/10.1002/ente.201900950>
25. Zhang T, Qu H, Sun K, Li S (2019) Facile fabrication of co-doped carbon matrix as sodium-ion battery anode. *ChemElectroChem* 6: 1776–1783. <https://doi.org/10.1002/celec.201801843>
26. Jiang J, Nie P, Fang S, Zhang Y, An Y, Fu R, Dou H, Zhang X (2018) Boron and nitrogen dual-doped carbon as a novel cathode for high performance hybrid ion capacitors. *Chin Chem Lett* 29: 624–628. <https://doi.org/10.1016/j.cclet.2018.01.029>
27. Hummers W, Offeman E (1985) *J Am Chem Soc* 80:1339
28. Wang C, Zhang X, Wang J, Ma Y, Lv S, Xiang J, Chu M, Sun T, Qin C (2018) Boron/nitrogen/oxygen co-doped carbon with high volumetric performance for aqueous symmetric supercapacitors. *J Electrochem Soc* 165:A856–A866. <https://doi.org/10.1149/2.0321805jes>
29. Li R, Qin C, Zhang X, Lin Z, Lv S, Jiang X (2019) Boron/nitrogen co-doped carbon synthesized from waterborne polyurethane and graphene oxide composite for supercapacitors. *RSC Adv* 9:1679–1689. <https://doi.org/10.1039/c8ra09043b>
30. Song P, He X, Shen X, Sun Y, Li Z, Yuan A, Zhai L, Zhang D (2019) Dissolution-assistant all-in-one synthesis of N and S dual-doped porous carbon for high-performance supercapacitors. *Adv Powder Technol* 30:2211–2217. <https://doi.org/10.1016/j.apt.2019.07.001>
31. Pattanauwat P, Thammasaroj P, Nuanwat W, Qin J, Potiyaraj P (2018) One-pot method to synthesis polyaniline wrapped graphene aerogel/silver nanoparticle composites for solid-state supercapacitor devices. *Mater Lett* 217:104–108. <https://doi.org/10.1016/j.matlet.2018.01.058>
32. Xu RX, Zhao YP, Liu GH, Zhu JS, Wang RY, Cao JP, Wei XY (2020) N/O co-doped porous interconnected carbon nanosheets from the co-hydrothermal treatment of soybean stalk and nickel nitrate for high-performance supercapacitors. *J Colloid Interface Sci* 558:211–219. <https://doi.org/10.1016/j.jcis.2019.09.097>
33. Zhang X, Wang Y, Du Y, Qing M, Yu F, Tian ZQ, Shen PK (2019) Highly active N,S co-doped hierarchical porous carbon nanospheres from green and template-free method for super capacitors and oxygen reduction reaction. *Electrochim Acta* 318:272–280. <https://doi.org/10.1016/j.electacta.2019.06.081>
34. Ni L, Wang R, Wang H, Sun C, Sun B, Guo X, Jiang S, Shi Z, Jing W, Zhu L, Qiu S, Zhang Z (2018) Designing nanographitic domains in N-doped porous carbon foam for high performance supercapacitors. *Carbon* 139:1152–1159. <https://doi.org/10.1016/j.carbon.2018.07.057>
35. Wang J-G, Liu H, Sun H, Hua W, Wang H, Liu X, Wei B (2018) One-pot synthesis of nitrogen-doped ordered mesoporous carbon spheres for high-rate and long-cycle life supercapacitors. *Carbon* 127:85–92. <https://doi.org/10.1016/j.carbon.2017.10.084>
36. Guo D, Xin R, Zhang Z, Jiang W, Hu G, Fan M (2018) N-doped hierarchically micro- and mesoporous carbons with superior performance in supercapacitors. *Electrochim Acta* 291:103–113. <https://doi.org/10.1016/j.electacta.2018.08.109>
37. Guo D, Qian J, Xin R, Zhang Z, Jiang W, Hu G, Fan M (2019) Facile synthesis of nitrogen-enriched nanoporous carbon materials for high performance supercapacitors. *J Colloid Interface Sci* 538: 199–208. <https://doi.org/10.1016/j.jcis.2018.11.107>
38. Guo D, Xin R, Wang Y, Jiang W, Gao Q, Hu G, Fan M (2019) N-doped carbons with hierarchically micro- and mesoporous structure derived from sawdust for high performance supercapacitors. *Microporous Mesoporous Mater* 279:323–333. <https://doi.org/10.1016/j.micromeso.2019.01.003>
39. Li Y, Wang G, Wei T, Fan Z, Yan P (2016) Nitrogen and sulfur co-doped porous carbon nanosheets derived from willow catkin for supercapacitors. *Nano Energy* 19:165–175. <https://doi.org/10.1016/j.nanoen.2015.10.038>
40. Wu X, Xing W, Florek J, Zhou J, Wang G, Zhuo S, Xue Q, Yan Z, Kleitz F (2014) On the origin of the high capacitance of carbon derived from seaweed with an apparently low surface area. *J Mater Chem A* 2:18998–19004. <https://doi.org/10.1039/c4ta03430a>
41. Miao L, Zhu D, Liu M, Duan H, Wang Z, Lv Y, Xiong W, Zhu Q, Li L, Chai X, Gan L (2018) N, S co-doped hierarchical porous carbon rods derived from protic salt: facile synthesis for high energy density supercapacitors. *Electrochim Acta* 274:378–388. <https://doi.org/10.1016/j.electacta.2018.04.100>
42. Wu X, Zhou J, Xing W, Zhang Y, Bai P, Xu B, Zhuo S, Xue Q, Yan Z (2015) Insight into high areal capacitances of low apparent surface area carbons derived from nitrogen-rich polymers. *Carbon* 94: 560–567. <https://doi.org/10.1016/j.carbon.2015.07.038>
43. Li H, Wu X, Zhou J, Liu Y, Huang M, Xing W, Yan Z, Zhuo S (2019) Enhanced Supercapacitive performance of MnCO₃@rGO in an electrolyte with KI as additive. *ChemElectroChem* 6:316–319. <https://doi.org/10.1002/celec.201801290>
44. Jiu H, Jiang L, Gao Y, Zhang Q, Zhang L (2019) Synthesis of three-dimensional graphene aerogel-supported NiCo₂O₄ nanowires for supercapacitor application. *Ionics* 25:4325–4331. <https://doi.org/10.1007/s11581-019-02970-1>
45. Zhang X, Gao X, Wu Z, Zhu M, Jiang Q, Zhou S, Huang Y, Rao Z (2019) High-capacitance supercapacitor based on nitrogen-doped porous carbons-sandwiched graphene hybrid frameworks. *Ionics* 25:6017–6023. <https://doi.org/10.1007/s11581-019-03154-7>
46. Wang L, Zhu Q, Zhao J, Guan Y, Liu J, An Z, Xu B (2019) Nitrogen-doped hierarchical porous carbon for supercapacitors with high rate performance. *Microporous Mesoporous Mater* 279: 439–445. <https://doi.org/10.1016/j.micromeso.2019.01.034>
47. Chang Y, Yuan C, Liu C, Mao J, Li Y, Wu H, Wu Y, Xu Y, Zeng B, Dai L (2017) B, N co-doped carbon from cross-linking induced self-organization of boronate polymer for supercapacitor and oxygen reduction reaction. *J Power Sources* 365:354–361. <https://doi.org/10.1016/j.jpowsour.2017.08.106>
48. Dahal B, Mukhiya T, Ojha GP, Muthurasu A, Chae S-H, Kim T, Kang D, Kim HY (2019) In-built fabrication of MOF assimilated B/N co-doped 3D porous carbon nanofiber network as a binder-free electrode for supercapacitors. *Electrochim Acta* 301:209–219. <https://doi.org/10.1016/j.electacta.2019.01.171>
49. Tai Z, Yan X, Xue Q (2012) Shape-alterable and -recoverable graphene/polyurethane bi-layered composite film for supercapacitor electrode. *J Power Sources* 213:350–357. <https://doi.org/10.1016/j.jpowsour.2012.03.086>